JPhys Energy

High performance composite Pr4Ni3O10±δ - Ce0.75Gd0.1Pr0.15O2−δ solid oxide cell air electrode

To cite this article before publication: Zheng Xie *et al* 2023 *J. Phys. Energy* in press https://doi.org/10.1088/2515-7655/aceeb5

High performance composite $Pr_4Ni_3O_{10\pm\delta}$ - $Ce_{0.75}Gd_{0.1}Pr_{0.15}O_{2-\delta}$ solid oxide cell air electrode

Zheng Xie[1], Inyoung Jang[2], Mengzheng Ouyang[3], Anna Hankin[2], and Stephen J Skinner*[1]

[1]Department of Materials, Imperial College London, London, SW7 2AZ, UK
[2]Department of Chemical Engineering, Imperial College London, SW7 2AZ, UK
[3]Department of Earth Science and Engineering, Imperial College London, SW7 2AZ, UK

1 Abstract

A composite electrode composed of $Pr_4Ni_3O_{10\pm\delta}$ - $Ce_{0.75}Gd_{0.1}Pr_{0.15}O_{2-\delta}$ (50 $wt.$ % - 50 $wt.$ %) was thoroughly investigated in terms of the electrochemical performance as a function of microstructure. The electrochemical performance was characterized by electrochemical impedance spectroscopy and the microstructures, characterized by focused ion beam-scanning electron microscopy and 3D reconstructions, were modified by changing the particle size of $Pr_4Ni_3O_{10\pm\delta}$ and the electrode thickness. The distribution of relaxation time (DRT) method was applied to help resolve electrochemical processes occurring in the electrodes. It was found that an appropriate increase in electrode thickness and an appropriate decrease in particle size enhanced the oxygen reduction reaction kinetics. The lowest area specific resistance obtained in this study at 670 $^{\circ}C$ under pO_2 of 0.21 atm was 0.055 Ω cm^2. Finally, a comparison to the Adler Lane Steele (ALS) model was made and the main active site for the oxygen reduction reaction was concluded to be triple phase boundaries. A fuel cell made of the composite material as the cathode was fabricated and tested. The peak power density was 1 Wcm^{-2} at 800 $^{\circ}C$, which demonstrates this composite material is promising for SOFC cathodes.

2 Introduction

The hydrogen economy, defined as the industrial system in which hydrogen is oxidized to water that could be reused for water electrolysis into oxygen and hydrogen by providing external energy, is an overwhelming development trend considering the current condition of energy shortage and environmental pollution [1, 2]. High temperature solid oxide fuel cells play an important role in this system, converting the chemical energy of hydrogen and derived products like ammonia into electrical energy with high efficiency, modularity and fuel flexibility [3, 4, 5]. However, the high operation temperatures accelerate cell degradation and restrict materials selection for cells [6]. Therefore, operation temperatures must be lowered to intermediate temperatures of around 600 - 800 $^{\circ}C$ to mitigate such issues. The associated issues with lowering operation temperatures are slow kinetics of electrode reactions and greater ohmic loss from oxygen ion diffusion in the electrolyte since these processes are temperature activated [6]. Technically, there are two methods to solve these issues: (a) optimization of the microstructures of cell; (b) applying innovative materials.

Microstructure optimization is mainly based on tailoring electrode microstructures to enhance the interface between the electrode and electrolyte. For instance, the kinetics of oxygen reduction reaction (ORR) occurring on the cathode could be enhanced by applying a well designed composite cathode, which is achieved by extending the triple phase boundary (TPB) from the electrolyte/electrode interface into the bulk electrode [7, 8, 9, 10, 11, 12]. The interface between the electrode and electrolyte can be improved by applying advanced deposition techniques [13, 14, 15] and addition of an interlayer[14, 16, 17, 18].

*Corresponding author. Tel.: +44 (0)20 7594 6782
Email address: s.skinner@imperial.ac.uk (S.J. Skinner)

Innovative materials have to possess excellent intrinsic properties under this intermediate temperature range [19]. For electrode materials, the key property is mixed electronic and ionic conductivity. With applying mixed electronic and ionic conductors as cathode materials, ORR can occur via a double phase boundary (DPB) route in the cathode which makes use of the entire surface of electrode particles[20, 21]. From the perspective of electrodes, the key factor in both methods is to extend active sites for electrode reactions.

$Pr_4Ni_3O_{10\pm\delta}$ (PNO), a member of the Ruddlesden - Popper series of materials, possesses high electronic conductivity and moderate ionic conductivity. A few groups investigated its structure and properties [22, 23, 24] and Vibhu et al. have identified PNO as a promising cathode for intermediate temperature solid oxide fuel cells (IT - SOFCs) [25]. In this article, PNO was mixed with $Ce_{0.75}Gd_{0.1}Pr_{0.15}O_{2-\delta}$ (CGPO), a good ionic conductor along with slight electronic conductivity due to doping of Pr [26], as a composite cathode for investigation of their electrochemical performances as a function of microstructure. The addition of an ionic conducting phase is to create more TPB for ORR. PNO and CGPO with a ratio of 50 $wt.$ % - 50 $wt.$ % was applied since this composition presented the lowest area specific resistance (ASR) among a variety of compositions according to previous investigations [27].

Based on this composition, the aim of this work was to optimize the electrode performance with introduction of active sites by increasing the electrode thickness and applying smaller PNO particles. The distribution of relaxation time (DRT) method was applied to help resolve electrochemical processes occurring in the electrodes. The evolution of each process as a function of microstructure, extracted from 3D reconstructions, was investigated.

3 Experimental section

PNO and CGPO powders were synthesized via a sol-gel route by dissolving stoichiometric amounts of metal nitrates into 10 $wt.$ % citric acid solution and heating on a hot plate with a magnetic stirrer at 300 $^{\circ}C$ and 200 rpm until a viscous solution formed. The viscous solution and beaker were transferred to a furnace and decomposed at 600 $^{\circ}C$ for 12 h with 2 $^{\circ}C\ min^{-1}$ heating and cooling. CGPO was obtained through this thermal treatment. For PNO, the decomposed solid precursor had to be calcined under O_2 flow at 1050 $^{\circ}C$ for 12 h with 5 $^{\circ}C\ min^{-1}$ heating and cooling. PNO was obatined by repeating this process 7 times with intermediate grinding [24]. $Zr_{0.809}Sc_{0.182}Ce_{0.009}O_2$ (10Sc1CeSz) powder (Lot No.H2228) for the interlayer was purchased from DKKK, Japan. It was sintered at 1500 $^{\circ}C$ for 5 h with 10 $^{\circ}C\ min^{-1}$ heating and cooling to obtain a single phase. Electrolyte pellets (Lot No.21AN02199), 10 $\pm$ 0.5 mm in diameter and 150 $\pm$ 15 um for thickness, were purchased from Kerafol, Germany. Gold paste (Gwent Group, Code No. C2090908D1) was used for the current collecting layer in subsequent electrochemical measurements. All materials were characterized by x-ray diffraction (PANalytical X'Pert Pro MPD with a Cu K_α source).

As prepared PNO was ball milled for 72 h to break agglomerates followed by high energy planetary ball milling. High energy planetary ball milling was applied to produce smaller PNO particles. Zirconia balls with a range of sizes were mixed PNO powder and immersed in ethanol. A reverse rotation mode was used and milling lasted 12 h at 300 rpm. The resulting powder was called milled PNO. The milled PNO was further milled with another set of milling agents to obtain even smaller particles, termed as 2nd milled PNO. In the following, for the sake of simplicity, we use UM, M and MM to represent the electrode composed of unmilled PNO, milled PNO and 2nd milled PNO, respectively. X-ray diffraction (XRD) was applied to examine the phase purity of the resulting powders.

Brunauer-Emmett-Teller (BET) test was carried out to confirm if the PNO particle size was effectively reduced by ball-milling. The surface area of the PNO powders was calculated using N_2 adsorption-desorption isotherms measured on a Micrometrics TriStar 3000 instrument by applying the Brunauer–Emmett–Teller equation. Prior to testing, approximately 250 mg of the powder samples were degassed under N_2 at 350 $^{\circ}C$ overnight to remove any residual solvents from the synthesis process.

Ball milling for 72 h was applied to break agglomerates of as prepared powder before preparing the electrode and interlayer ink. High energy planetary milled powders were directly applied in preparing the ink. The electrode ink was prepared by mixing the same weight of PNO powder, CGPO powder, and commercial ink vehicle (Fuel Cell Materials, USA, #311006) followed by triple-roll milling (EXAKT 80E) for homogeneous distribution and cracking of agglomerates. Hence, the weight ratio of powders to ink vehicle was 2 : 1. In analogy to electrode ink preparation, interlayer

ink (10Sc1CeSz) was prepared with the same weight ratio. Interlayer ink was screen printed on each side of the pellet followed by sintering at 1500 $^{\circ}C$ for 2 h with 10 $^{\circ}C\ min^{-1}$ for heating and cooling. All symmetrical cells were based on such an electrolyte with an interlayer on both sides. The addition of an interlayer was to increase the roughness of the pellet for better adhesion between the pellet and the electrode. Next, the electrode ink was screen printed on the interlayer of each side followed by sintering at 900 $^{\circ}C$ for 2 h with 2 $^{\circ}C\ min^{-1}$ heating and cooling. The electrode was 6 mm in diameter (0.2826 cm^2) and three different thicknesses were obtained by adjusting printing parameters. After electrode deposition, gold paste was brush painted on the electrode of each side followed by sintering at 700 $^{\circ}C$ for 2 h with 5 $^{\circ}C\ min^{-1}$ heating and cooling.

The as prepared symmetrical cell was characterized by electrochemical impedance spectroscopy (EIS) with a frequency response analyser (Solartron 1260a Impedance/Gain-Phase Analyser). EIS measurements at temperatures ranging from 625 $^{\circ}C$ to 717 $^{\circ}C$ and under pO_2 of from 0.005 atm to 0.23 atm were carried out to study the electrochemical performance of the composite electrodes with different thicknesses and different PNO particle sizes. The EIS setup was as follows: 50 mV AC voltage, frequency range from 1 $M\ Hz$ to 0.05 Hz with 30 points measured per decade and 3 s integration time. In some cases, 10 points measured per decade was applied in the low frequency region. 2.5 h delay time was applied before each EIS measurement to allow samples to reach an equilibrium state.

The thickness of composite electrodes was measured under scanning electron microscopy (SEM) (Zeiss Auriga FIB - SEM). Focused ion beam - scanning electron microscopy(FIB - SEM) (Zeiss Auriga FIB - SEM) was applied to investigate the microstructures of composite electrodes. The relevant parameters can be found in Supporting Information. The obtained images were analyzed by Avizo to extract microstructure parameters and tortuosity of each phase was extracted from the MATLAB plug-in TauFactor[28].

With respect to fuel cell fabrication, nickel oxide (NiO) - yttria stabilised zirconia (YSZ) anode (negative) support substrate was prepared via the pelletization method. NiO powder and YSZ powders were (NiO-S, YSZ8-U5, Fuelcellmaterials, USA) prepared and mixed with pore former through a ball-milling method in the ethanol solvent for 24 h, on the roller mixer. A mixture of 3 mm and 5 mm diameter size of zirconia balls for used as a ball milling medium, and after 24 h of mixing, the mixed solution was dried separately in the 70 $^{\circ}C$ drying oven. After completely drying the solvent, the mixture was lightly ground using a pestle and mortar. The obtained powder was pelletized using a pellet die (25 mm diameter size). The fabricated anode support pellets were pre-sintered at 900 $^{\circ}C$ for 5 h with a ramping rate of 5 $^{\circ}C\ min^{-1}$.

After the pre-sintering process, the YSZ electrolyte layer was dip-coated on the surface of the pellet via the dip-coating method. The YSZ electrolyte layer dip-coating solution was prepared following the method reported in the published work [29]. One side of the anode support was covered with the organic film and dipped in the solution and dragged out, subsequently followed by a heat treatment at 600 $^{\circ}C$ to remove the organic film and organic materials remaining in the dip-coating solution. The heat-treated substrate was fully sintered at 1450 $^{\circ}C$ for 5 h for obtaining gas-tight dense electrolyte on one side. After the sintering, a GDC layer was covered on the YSZ layer using the same dip-coating method and heat-treated at 1200 $^{\circ}C$ for 2 h to give enough adhesion property on the YSZ. Afterward, cathode pasted composed of CGPO and unmilled PNO was applied on the surface of GDC interlayer and heat-treated at 800 $^{\circ}C$ for 2 h with a heating and cooling rate of 2 $^{\circ}C\ min^{-1}$.

The electrochemical performance was evaluated using a prepared anode-supported solid oxide cell. The cell was sealed on one end of the alumina tube for feeding the hydrogen on the anode support side, by facing the negative electrode part towards the alumina tube and sealed using a ceramic paste (Adhesive 668, Aremco, USA). The silver paste and silver mesh were applied on the surface of the positive electrode layer as a current collector, and the Pt wire was connected on the surface as a connection wire led to the potentiostat ((PGSTAT302N, Metrohm, The Netherlands).

The electrochemical performance in fuel cell mode was evaluated at four temperature conditions: 650 $^{\circ}C$, 700 $^{\circ}C$, 750 $^{\circ}C$, and 800 $^{\circ}C$. Before starting the testing, the cell was reduced with 10 % hydrogen at 600 $^{\circ}C$ for overnight. The air was flown on the cathode side with 200 *sccm* while testing and 100 *sccm* of wet hydrogen on the anode side. The current-potential measurement was done from open circuit voltage (OCV) to 0.1 V for its fuel cell performance testing, and impedance was measured at OCV condition with the frequency range of 0.1 $M\ Hz - 0.1\ Hz$ at each operation temperature.

4 Results and discussion

4.1 XRD

Each of the materials prepared for the electrochemical testing was characterized by XRD and was confirmed as a single phase. As prepared CGPO and CGPO after 72 h ball milling are shown in figure. S2. Thermally treated 10Sc1CeSz for the interlayer and purchased pellets are shown in figure. S3. As prepared PNO and 72 h ball milled PNO are shown in figure. S4. PNO after planetary ball milling was also characterized, as shown in figure. S4c and S4d.

The XRD patterns of the electrode before and after EIS measurements are illustrated in figure. S5. No secondary phase except NiO is observed after EIS measurement, which is consistent with what Tsai [27] reported. NiO is observed in both patterns as a result of cation diffusion at the interface between PNO and CGPO phase during sintering at 900 $^{\circ}C$. There is no reactivity between PNO and 10Sc1CeSz during sintering and EIS measurement [27]. Although there is cation diffusion from CGPO to 10Sc1CeSz forming a solid solution during sintering, the reactivity between CGPO and 10Sc1CeSz during EIS measurements can be neglected considering the temperature and time scale [27]. The electrode characterized by XRD was removed from the pellet so a small amount of both the electrolyte and current collector are observed in the diffraction data.

4.2 SEM

The thickness of the electrodes was controlled by the thickness of the mask used during screen printing and was separated into three different thicknesses which were confirmed by scanning electron microscopy (SEM), as shown in figure. S7. For the sake of simplicity, the thinnest, medium and thickest electrodes are described as T1, T2 and T3, respectively. For example, T1UM represents an electrode of 16 $\pm$ 1.5 um composed of CGPO and unmilled PNO. All samples are summarized in table. 1.

Abbreviation	Thickness	PNO particles
T1UM/T1M/T1MM	16 $\pm$ 1.5um	unmilled PNO/milled PNO/2nd milled PNO
T2UM/T2M/T2MM	36 $\pm$ 3.8um	unmilled PNO/milled PNO/2nd milled PNO
T3UM/T3M	50 $\pm$ 2.8um	unmilled PNO/milled PNO

Table 1: Electrode thicknesses of different samples

4.3 FIB - SEM

3D volumes for electrodes composed of unmilled, milled and 2nd milled PNO phase were constructed by stacking hundreds of FIB - SEM images, as shown in figure. 1a, figure. 1c and figure. 1e. It can be observed that many PNO particles were reduced from micron-scale to nano-scale after milling, although some micron-scale particles were still present. After the 2nd milling, the PNO particles were even smaller and virtually no micron-scale particles were observed. The smaller particle size was also confirmed by dynamic light scattering, as shown in figure. S1, and BET result as shown in table. S1, as well as peak broadening effects observed in the XRD patterns shown in figure. S4. table. 2 summarizes all of the microstructural parameters of electrodes composed of unmilled, milled and 2nd milled PNO. The particle size of PNO was significantly reduced to 504 nm from 1240 nm after milling, and to 313 nm after the 2nd milling. The deposited electrode had higher TPB and DPB density when using smaller PNO as one of its components.

Total and active TPB density are included in table. 2. TPB is active only when the continuous paths for each phase are guaranteed [6]. Active TPB density increased to 6.6 um^{-2} from 4.6 um^{-2} after milling the PNO phase and further increased to 9.1 um^{-2} after 2nd milling. The values of active TPB density are close to the values reported in previous investigations, around 5–10 um^{-2} [30, 31, 32]. The active TPB skeletons within electrodes composed of different PNO are illustrated in figure. 1b, 1d and 1f. The same applies to DPB. Active DPB density increased from 138 um^{-1} to 212 um^{-1} and further to 263 um^{-1} when milled PNO and 2nd milled was applied, respectively. The tortuosity of the PNO phase almost doubled from unmilled PNO to milled PNO, which was reasonable because smaller particle size resulted in a more dispersive distribution. The tortuosity of the electrode composed of 2nd milled PNO was 50 $\pm$ 5. The tortuosity of CGPO slightly increased to 3.3 $\pm$ 0.5 from 2.3 $\pm$ 0.2, and then to 5.5 $\pm$ 0.9 with decreasing the PNO size, possibly resulting from the interruption of connected paths caused by the significantly dispersive distribution of smaller

PNO particles. This is supported by considering the average coordination number of each particle [33]. The average number of contacts of a CGPO particle with neighboring CGPO particles is given by Eq. 1, where Z_0 is the average coordination number of all particles and has a value of 6 for a binary random packing of spheres. S is the surface-area fraction of CGPO particles, which is related to the volume fraction φ and particle radius r, as shown in Eq. 2. Subscript i and e represent the ionic and the electronic phase, respectively. As the PNO particle size is reduced, the surface-area fraction of CGPO is expected to decrease and hence, the average number of contacts of a CGPO particle with neighboring CGPO particles decreases.

$$Z = Z_0 S \tag{1}$$

$$S = \frac{\varphi_i / r_i}{\varphi_i / r_i + \varphi_e / r_e} \tag{2}$$

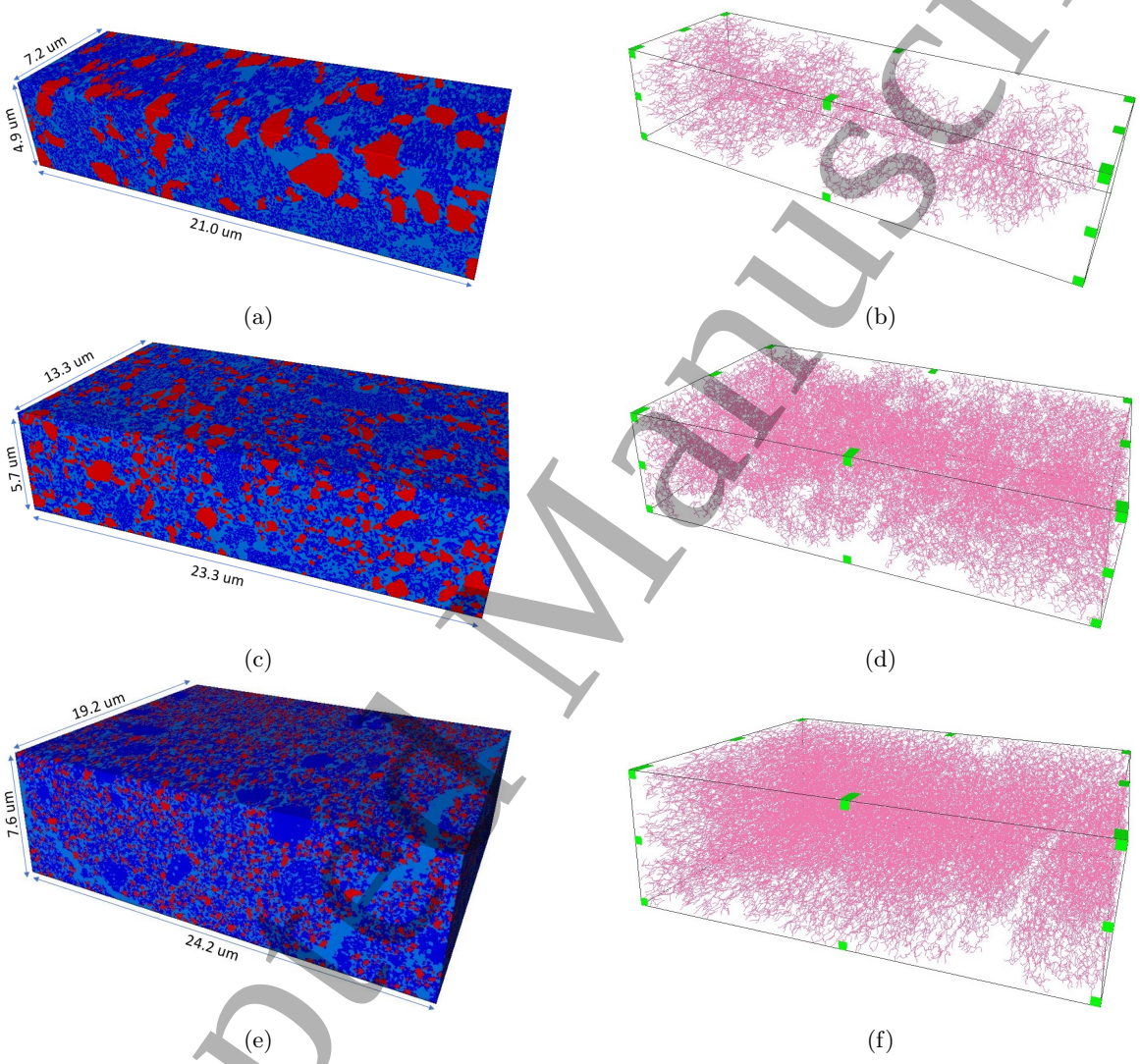

Figure 1: 3D volume-rendering of analyzed sample volume for electrode composed of CGPO and (a) unmilled PNO, (c) milled PNO, (e) 2nd milled PNO (Red phase represents PNO, light and dark blue phases represent pore and CGPO, respectively. Corresponding active TPB skeleton network for electrodes composed of CGPO and (b) unmilled, (d) milled PNO, (f) 2nd milled PNO, respectively.

Sample	unmilled	milled	2nd milled
Average particle size PNO (nm)	1240 ± 40	504 ± 46	313 ± 25
Average particle size Pore(nm)	55 ± 5	46 ± 10	54 ± 5
Average particle size CGPO(nm)	46 ± 6	42 ± 14	48 ± 1
Total TPB density(um^{-2})	5.1 ± 0.5	7.0 ± 1.2	10.0 ± 1.6
Active TPB density(um^{-2})	4.6 ± 0.1	6.6 ± 1.2	9.1 ± 1.5
Total DPB density(um^{-1})	145 ± 17	222 ± 33	273 ± 61
Active DPB density(um^{-1})	138 ± 21	212 ± 39	263 ± 67
Tortuosity of PNO	19 ±1	40 ± 7	50 ± 5
Tortuosity of CGPO	2.3 ± 0.2	3.3 ± 0.5	5.5 ± 0.9

Table 2: Microstructural parameters for electrodes composed of CGPO and unmilled PNO, milled PNO, 2nd milled PNO. The volume fraction and tortuosity data were obtained from Taufactor [28] and the rest of the data were extracted from Avizo.

4.4 EIS

Electrodes were characterized by EIS under different oxygen partial pressures to determine what electrochemical processes were occurring within the electrodes. This is because the exponent n in the following expression, which describes how cathode polarization resistance changes as a function of oxygen partial pressure, helps determine elementary ORR occurring in electrodes, where k is a constant[34, 35, 36].

$$R = k(pO_2)^{-n} \tag{3}$$

where n relates to the following elementary oxygen reduction steps:

- $n = 1$, oxygen molecular adsorption

  $O_{2(g)} \rightarrow O_{2(ads)}$

- $n = 0.5$, oxygen molecular dissociation

  $O_{2(ads)} \rightarrow 2O_{ads}$

- $n = 0.25$, charge transfer

  $O_{ads} + 2e^{'} + V_o^{\cdot\cdot} \rightarrow O_o^X$

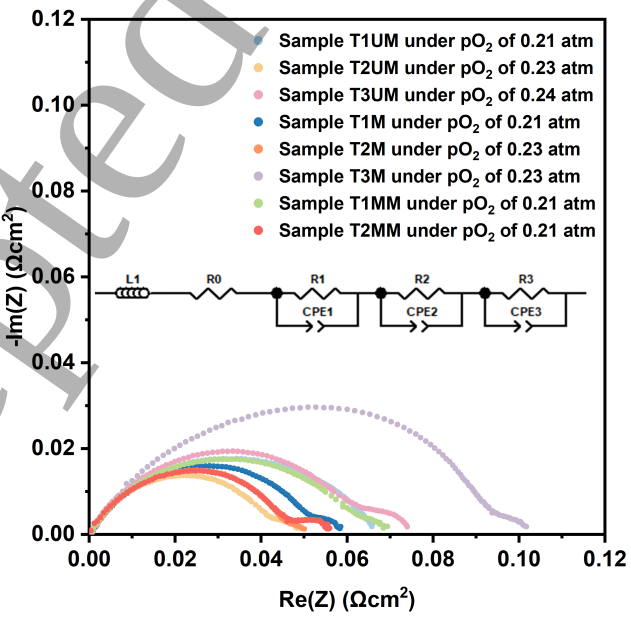

Figure 2: Nyquist plot for each sample under controlled oxygen partial pressure as indicated in the legend, at 670 $^{\circ}C$, with the applied equivalent circuit for fitting as an inset.

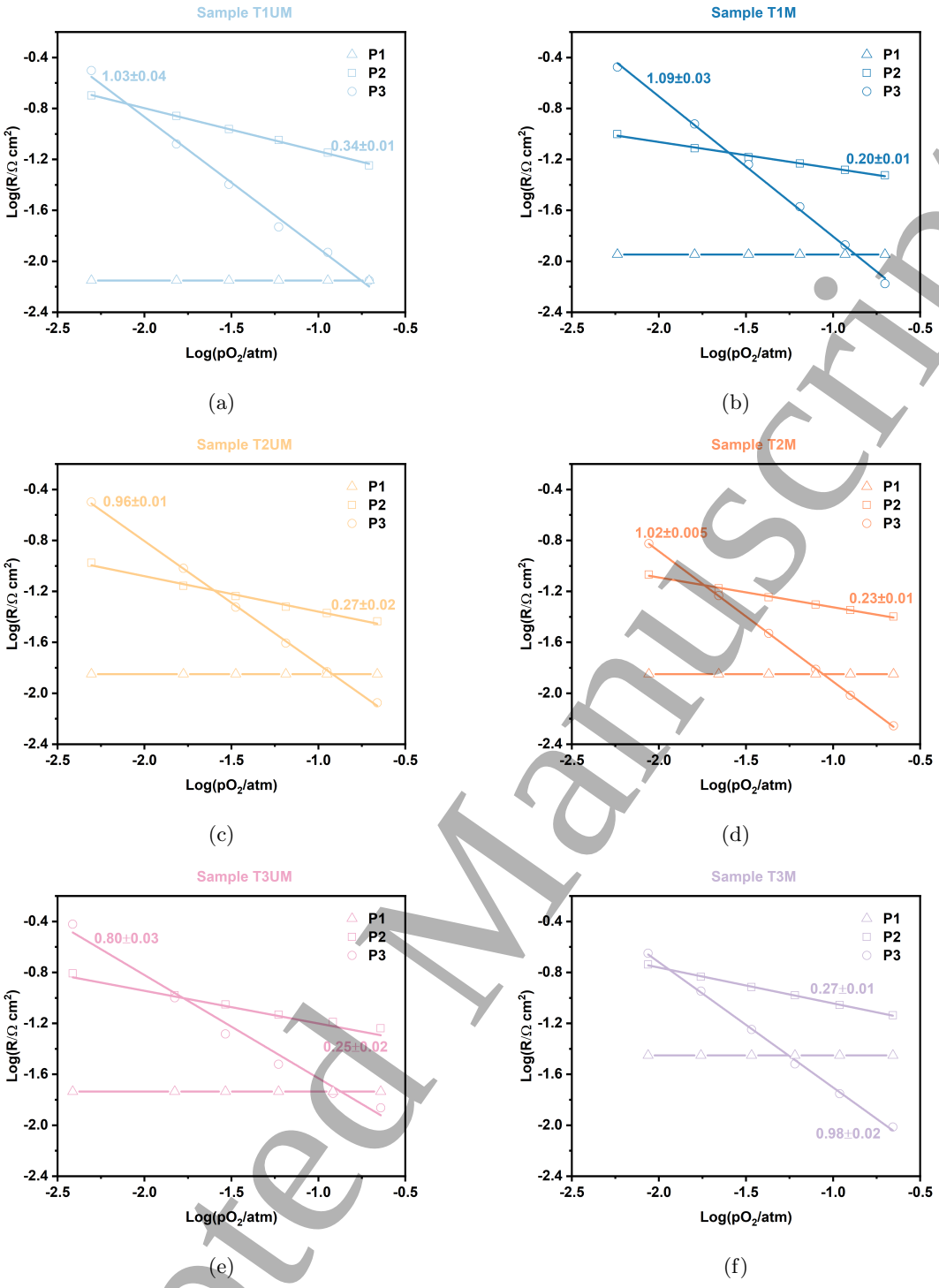

Figure 3: Dependence of resistance of each process for sample (a)T1UM, (b)T1M, (c)T2UM, (d)T2M, (e)T3UM), (f) T3M, on oxygen partial pressures measured at 670 $^{\circ}C$.

Nyquist plots of electrodes with different microstructures, measured at 670 $^{\circ}C$ under oxygen partial pressure of around 0.21 atm, are shown in figure. 2. The validity of the spectra was confirmed by Kramers-Kronig validity test by $Lin-KK$ tool [37, 38]. The intercept with the x-axis at high frequencies was normalized to the origin and inductance was truncated for better visualization. An equivalent circuit composed of three R//CPE elements connected in series with a resistor and an inductor, as shown in figure. 2 as an inset, was used to fit the Nyquist plot of each electrode. Residual plots between the measured spectra and the fitting results are given in figure S11. This indicated that there are at least three electrochemical processes P1, P2 and P3 from high frequencies ($\sim 10\,000\ Hz$) to low frequencies($\sim 1\ Hz$). The ASR of each process as a function of oxygen partial pressure, obtained from Nyquist plot fitting, is illustrated in figure. 3. Sample T1MM and sample

T2MM were only measured at 670°C under oxygen partial pressure of 0.21 atm. For more accurate identification of electrochemical processes [39], the distribution of relaxation time (DRT) was also calculated with a regularization parameter of 10^{-3} for each investigated sample, as shown in figure. 4. In total 5 peaks were observed for each sample, hence, there should be 5 electrochemical processes.

After inspecting the resistance and the characteristic frequency of each peak in DRT, it was found that the peak at the highest frequency and the peak at the lowest frequency corresponded to P1 and P3, respectively, while P2 consisted of three peaks, P2H, P2M and P2L. P2L accounted for $\sim$ 35 % of the overall resistance for sample T1UM under air, while it was negligible for the other five samples, as shown in figure. 4. An extra R//CPE element was added to the previous equivalent circuit, i.e. four R//CPE elements in series, to fit each Nyquist plot. However, the fitting results deviated far from a reasonable range. This was expected as the time constant of P2H and P2M was very close, and the resistance of P2L was quite small. Hence, we still used the equivalent circuit composed of three R//CPE elements to fit the Nyquist plots and extracted resistance values of P1, P2 and P3. The resistance of P2H, P2M and P2L were extracted by multiple peak fitting with Gaussian function with an example for sample T2UM given in figure. 4d. The peak fitting for other samples can be found in figure. S13 and figure. S14. The resistance of P2 was a sum of the resistance of P2H, P2M and P2L.

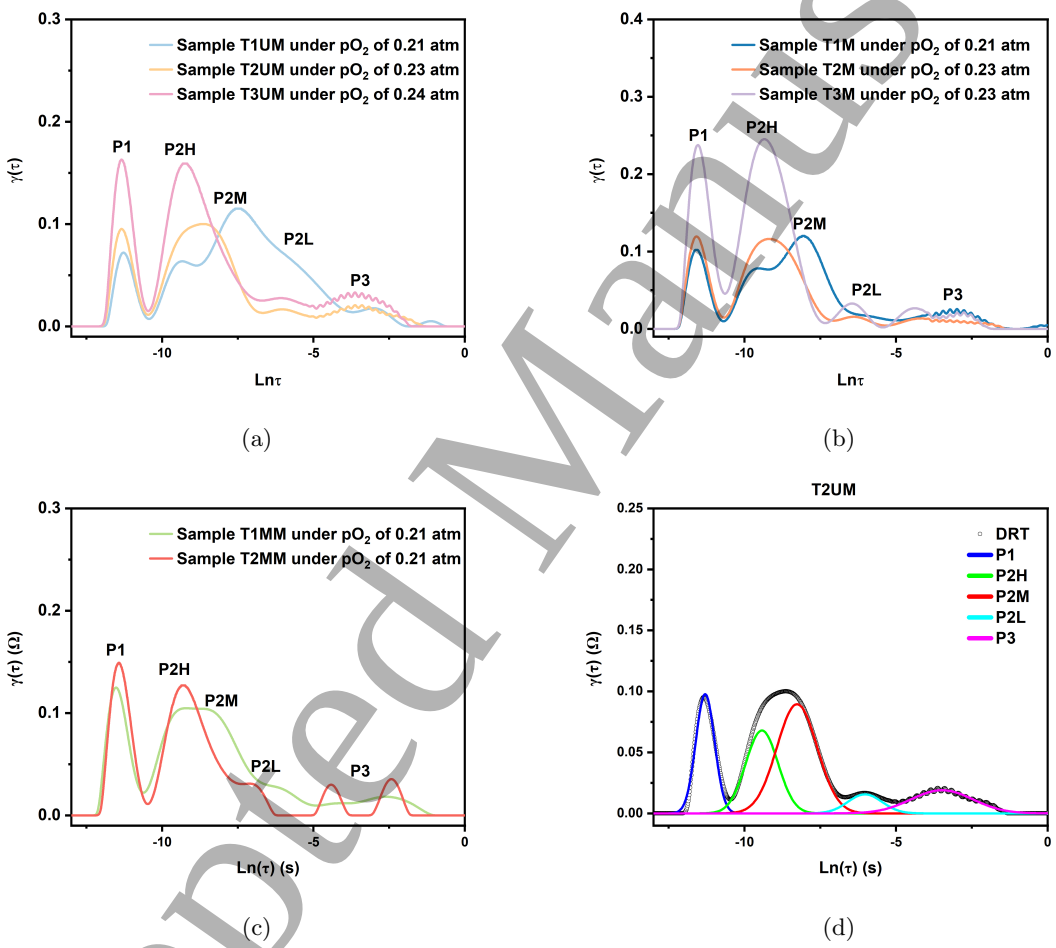

Figure 4: Distribution of relaxation time of samples composed of CGPO and (a) unmilled PNO with different thicknesses, (b) milled PNO with different thicknesses, (c) 2nd milled PNO with different thicknesses, measured at 670 °C. (d) Peak fitting for the sample T2UM with Gaussian function .

EIS as a function of temperature for all samples was also carried out and the DRT was performed. The DRT evolution with oxygen partial pressure and with temperature for sample T2UM is illustrated in figure. 5, which helps to visualize each process change as a function of oxygen partial pressure and temperature, especially P2H, P2M and P2L.

The resistance and capacitance of process P1 occurring at the highest frequency was virtually independent of oxygen partial pressure, as shown in figure. 5a. One possible assignment for this process is the oxygen ions transfer between interfaces [40, 41, 42]. It was more likely to be the oxygen

ion transfer between the composite electrode and the interlayer rather than between the interlayer and the electrolyte since both were the same material and the grain boundary effect was minimized due to sintering of the interlayer on the electrolyte at 1500 $^{\circ}C$ [43]. However, P1 should be attributed to oxygen ion diffusion in the CGPO phase within the electrode considering the capacitance of P1 $\sim 10^{-3}$ $F\ cm^{-2}$ [44, 45, 46, 47, 48]. The capacitance of each process as a function of oxygen partial pressure is illustrated in figure. S15. The activation energy of P1 was 1.00 ± 0.06 eV, given in figure. S16. This value was greater than the activation energy of ionic conductivity of around 0.5-0.6 eV for CGPO and $Ce_{0.9}Gd_{0.1}O_{1.95}$ reported in the literature [26, 49]. The discrepancy was probably because of the presence of contact resistance between CGPO particles.

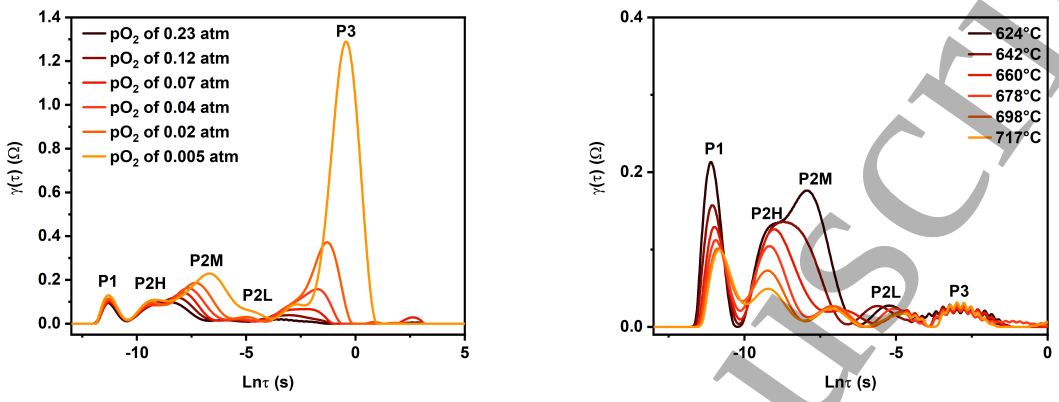

(a) (b)

Figure 5: Distribution of relaxation time for sample T2UM (a) under different oxygen partial pressures measured at 670 $^{\circ}C$, and (b) at different temperatures under pO_2 of 0.21 atm.

Similarly, the resistance of P2H was also independent of oxygen partial pressure. Since P2H was constant as a function of pO_2, the slope of P2 as a function of pO_2 was also the slope of P2M+P2L. According to the slope of P2M+P2L, P2M+P2L should be assigned to charge transfer at active sites since the slope -n was close to -0.25, as shown in Fig 3. However, considering the slope of the sample T1UM, -0.338, deviated from -0.25 and showed more oxygen molecular dissociation dependence which resulted from a significantly large resistance of P2L process in comparison with the other 5 samples, as shown in figure. 4, it was more reasonable to attribute P2M to charge transfer and P2L to oxygen molecular dissociation.

The capacitance of the process P2H was around 10^{-2} $F\ cm^{-2}$. It was associated with oxygen incorporation into the PNO phase followed by diffusion in the PNO phase within the electrodes. It is reasonable to assume the oxygen reduction processes: Firstly, the major oxygen molecules were adsorbed on the PNO surface. Then oxygen was dissociated, reduced and incorporated into the PNO phase due to its high oxygen exchange coefficient followed by diffusion to (1) the electrolyte, and (2) to the CGPO phase via TPB and then to the electrolyte. Since the processes P2H and P2M merged together at higher temperatures, as shown in figure. 5b, the activation energy of both could not be obtained. However, the activation energy of the process P2H+P2M was extracted, as shown in figure. S16. The single activation energy for the process P2H+P2M supported this assumption because most of the MIEC as electrodes are co-limited by surface exchange and bulk diffusion [20]. Huang et al. also observed similar peaks in investigating bismuth-based composite cathodes [47].

The lowest frequency process P3 was assigned to oxygen molecular adsorption because the slope -n was very close to -1. In addition, it was a temperature independent process as shown in figure. 5b which confirms the validity of the assignment. The difference in resistances of P3 between different samples was not discussed here since the difference in the resistance of P3 was negligible compared to the total ASR.

At 670 $^{\circ}C$, the sample T1UM presented the total ASR of 0.074 $\Omega\ cm^2$ under pO_2 of 0.21 atm, extracted from the fitted line in figure. 3. After increasing the electrode thickness to 36 um, the total ASR of sample T2UM reduced to 0.055 $\Omega\ cm^2$ which was the lowest ASR among all samples studied. This enhancement was expected since more active area was introduced into the electrode[50, 51]. This is also the case when an electrode composed of milled PNO phase had greater thickness, 0.065 $\Omega\ cm^2$ for sample T1M to 0.063 $\Omega\ cm^2$ for sample T2M measured at 670 $^{\circ}C$ under pO_2 of 0.21 atm, extracted from the fitted line in figure. 3. However, a further increase of the thickness of

the electrode to 50 um increased the ASR, even higher than the resistance for samples of 16 um thickness, which could possibly result from concentration polarization and higher resistances for transportation of oxygen ions and electrons. This was also observed in many previous investigations that study how electrode thickness affects the ORR [9, 10, 12, 52, 53].

Besides thickness adjustments, milling constituent particle size down also helped reduce ASR. By extracting the ASR under pO_2 of 0.21 atm from the fitted line, it can be found that the ASR of 0.074 $\Omega\ cm^2$ for sample T1UM was reduced to 0.065 $\Omega\ cm^2$ for sample T1M. The only difference between sample T1UM and T1M was a different size of PNO particles. Unlike enhancement achieved by increasing thickness to increase the active area, i.e. amount of TPB/DPB sites, this enhancement was achieved by greater TPB/DPB density under a given volume since smaller PNO phase with smaller particles created more TPB/DPB sites, consistent with the results obtained from FIB - SEM. Controlling the particle size of an electrode is a common way to lower its polarization resistance by extending TPB length [12, 33, 54, 55, 56, 57, 58]. However, for electrodes of 36 um thickness, sample T2UM has slightly lower total ASR than sample T2M, which was opposite to the expectation.

4.5 Discussion

The resistance value of each process of each sample, extracted from the peak fitting of the DRT, is plotted in figure. 6 and figure. 7 which illustrates how the resistance of each process changed with the electrode thickness and how the resistance of each process changed with the particle size of the constituent phase, respectively.

4.5.1 Effects of electrode thickness

It can be observed that the resistance of the process P2, measured at 670 $°C$ under pO_2 of around 0.21 atm, decreased significantly from the sample T1UM to the sample T2UM, as shown in figure. 6a. The major contribution to this was the reduction of the resistance of the process P2L, from 0.026 $\Omega\ cm^2$ to 0.003 $\Omega\ cm^2$ as shown in figure. 6c, which was associated with oxygen molecular dissociation. Although the resistance of the process P2H increased slightly, the total resistance decreased from 0.074 $\Omega\ cm^2$ to 0.055 $\Omega\ cm^2$. This resistance reduction confirmed that more TPB/DPB sites facilitate the ORR. When further increasing the thickness, both resistances of processes P1 and P2 increased. The increase in resistance of process P2 was mainly a result of an increase in that of process P2H, as shown in figure. 6c.

The sample composed of CGPO and milled PNO showed a similar change with thickness increase. From sample T1M to T2M, the resistance of process P2 decreased slightly. The resistance of process P2M decreased from 0.031 $\Omega\ cm^2$ to 0.023 $\Omega\ cm^2$, as shown in figure. 6d. However, most of the resistance reduction was compensated by an increase in the resistance of process P2H, from 0.011 $\Omega\ cm^2$ to 0.016 $\Omega\ cm^2$. In addition, the resistance of process P1 increased from 0.012 $\Omega\ cm^2$ to 0.016 $\Omega\ cm^2$, as shown in figure. 6b. Hence, the total resistance was almost the same, from 0.065 $\Omega\ cm^2$ to 0.063 $\Omega\ cm^2$, since the contribution from process P2M was compensated by the increase of the resistance of P1 and P2H. Likewise, both resistances of processes P1 and P2H increased dramatically when further increasing the electrode thickness to sample T3M. This increase was even greater compared to samples composed of CGPO and unmilled PNO. Hence, sample T3MM was not prepared and tested because it was expected to give higher resistances considering the trend observed.

Sample	Ohmic resistance (Ω)	Sample	Ohmic resistance (Ω)
Sample T1UM	7.1 ± 0.1	Sample T1M	6.6 ± 0.2
Sample T2UM	7.5 ± 0.1	Sample T2M	7.6 ± 0.2
Sample T3UM	9.0 ± 0.1	Sample T3M	9.0 ± 0.1

Table 3: Ohmic resistance of each sample at 670 $°C$ under pO_2 of around 0.21 atm. Ohmic resistance reported here includes contact resistance, rig resistance, and contributions from the interlayer and electrodes.

The increase of resistance of process P1 and P2H as increasing the electrode thickness can be explained considering the nature of processes P1 and P2H. Since both of them were related to oxygen species diffusion within the electrode, the longer diffusion path resulted in higher resistances. Apart from this, the ohmic resistance of each sample, extracted from the high frequency x-axis intercept of the Nyquist plots and listed in table 3, also gave us some information. The increment in electrode

thickness was around 20 *um* from T1 to T2, then to T3. The ohmic resistance increased 0.4 Ω from T1UM to T2UM and 1 Ω from T1M to T2M, respectively. This change increased dramatically to 1.5 Ω from T2UM to T3UM and 1.4 Ω from T2M to T3M, respectively. The ohmic resistance change indicated that below a thickness of 50 *um* (T3), the percolation of the electronic conducting phase (PNO), or the number of connected paths through the electrode, decreased with increasing the electrode thickness. The rate of decrease was faster at greater thickness. In analogy to the electronic conducting phase, the percolation of the ionic conducting phase (CGPO) was not ideal with increasing the electrode thickness, which resulted in higher resistances for oxide ion diffusion. This explains why the resistance of process P1 and process P2H increased with increasing electrode thickness and why the increase was greater with greater thickness.

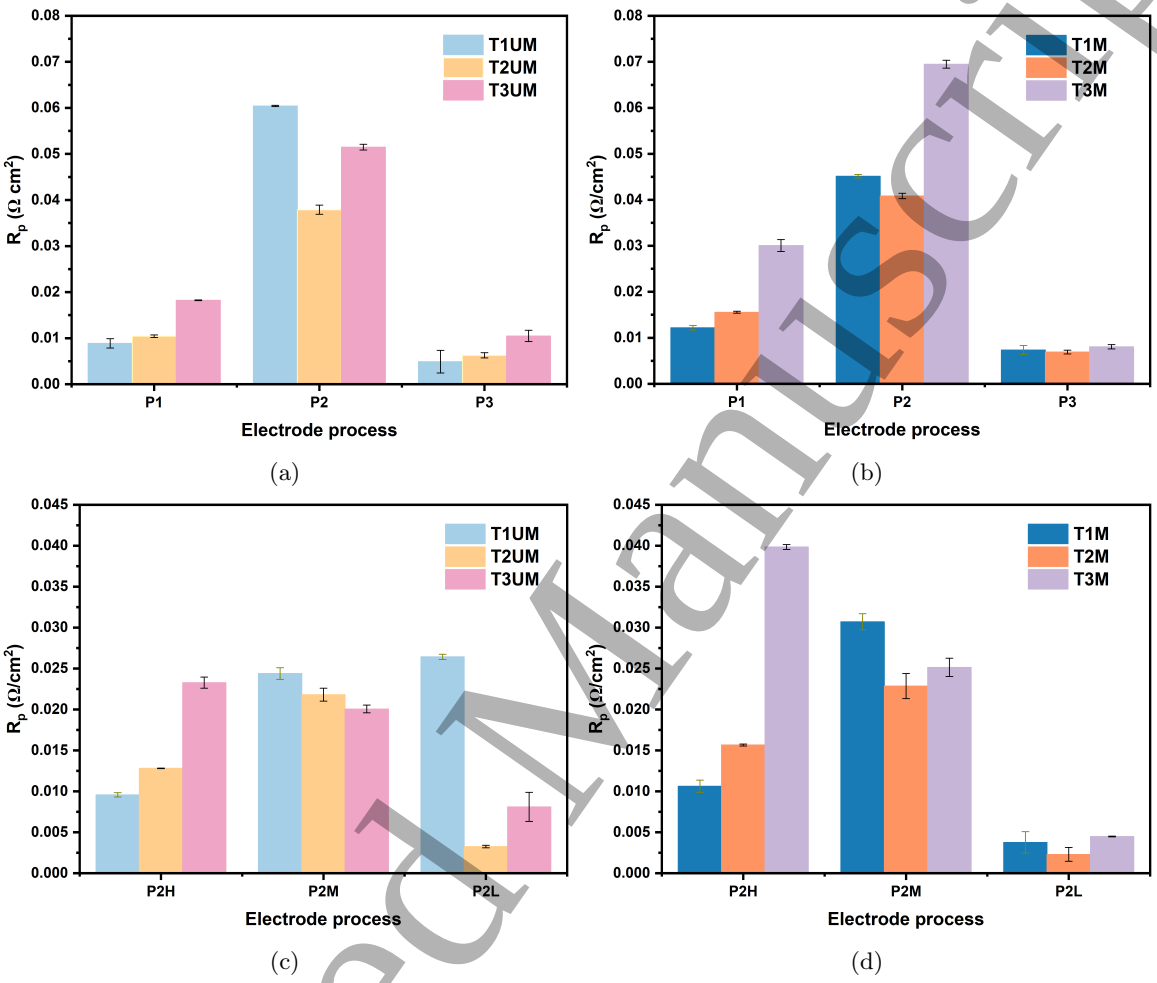

Figure 6: Polarization resistance of each process, extracted from peak fitting of distribution of relaxation time, for (a) the sample T1UM, T2UM and T3UM, (b) the sample T1M, T2M and T3M, measured at 670 $^{\circ}C$ under pO_2 of around 0.21 *atm*. The sub-processes of P2 of corresponding samples, P2H, P2M and P2L, were given in (c) and (d), respectively.

4.5.2 Effect of particle size

The smaller particle size of electrodes also facilitated the ORR as the resistance of process P2L decreased from 0.026 Ω cm^2 for sample T1UM to 0.004 Ω cm^2 for sample T1M measured at 670 $^{\circ}C$ under pO_2 of around 0.21 *atm*, as shown in figure. 7c. Although there was a minor increase in the resistance in processes P1 and P2M, the total resistance decreased from 0.074 Ω cm^2 to 0.065 Ω cm^2. When further milling the PNO particles size, the total resistance increased to 0.074 Ω cm^2 for sample T1MM, since the resistance of processes P1 and P2H increased, as shown in figure. 7a and figure. 7c.

For samples with electrode thickness of 36 *um*, the milled PNO had no benefit to each electrode process, as shown in figure. 7b. The resistance of process P1 increased from 0.010 Ω cm^2 for sample T2UM to 0.016 Ω cm^2 for sample T2M. For process P2H, the resistance increased from 0.013 Ω cm^2 for sample T2UM to 0.016 Ω cm^2 for sample T2M. The resistance of process P2M was virtually

the same for sample T2UM and sample T2M. However, the resistance of process P2H for sample T2MM was 0.013 $\Omega\ cm^2$ which was virtually the same as that for sample T2UM and the resistance of process P2M for sample T2MM was 0.016 $\Omega\ cm^2$ which was lower than that for sample T2UM and sample T2M. The resistance of process P1 for sample T2MM was the highest, of 0.019 $\Omega\ cm^2$, following the trend that smaller particle sizes resulted in higher resistance of process P1, observed in samples T1UM, T1M and T1MM.

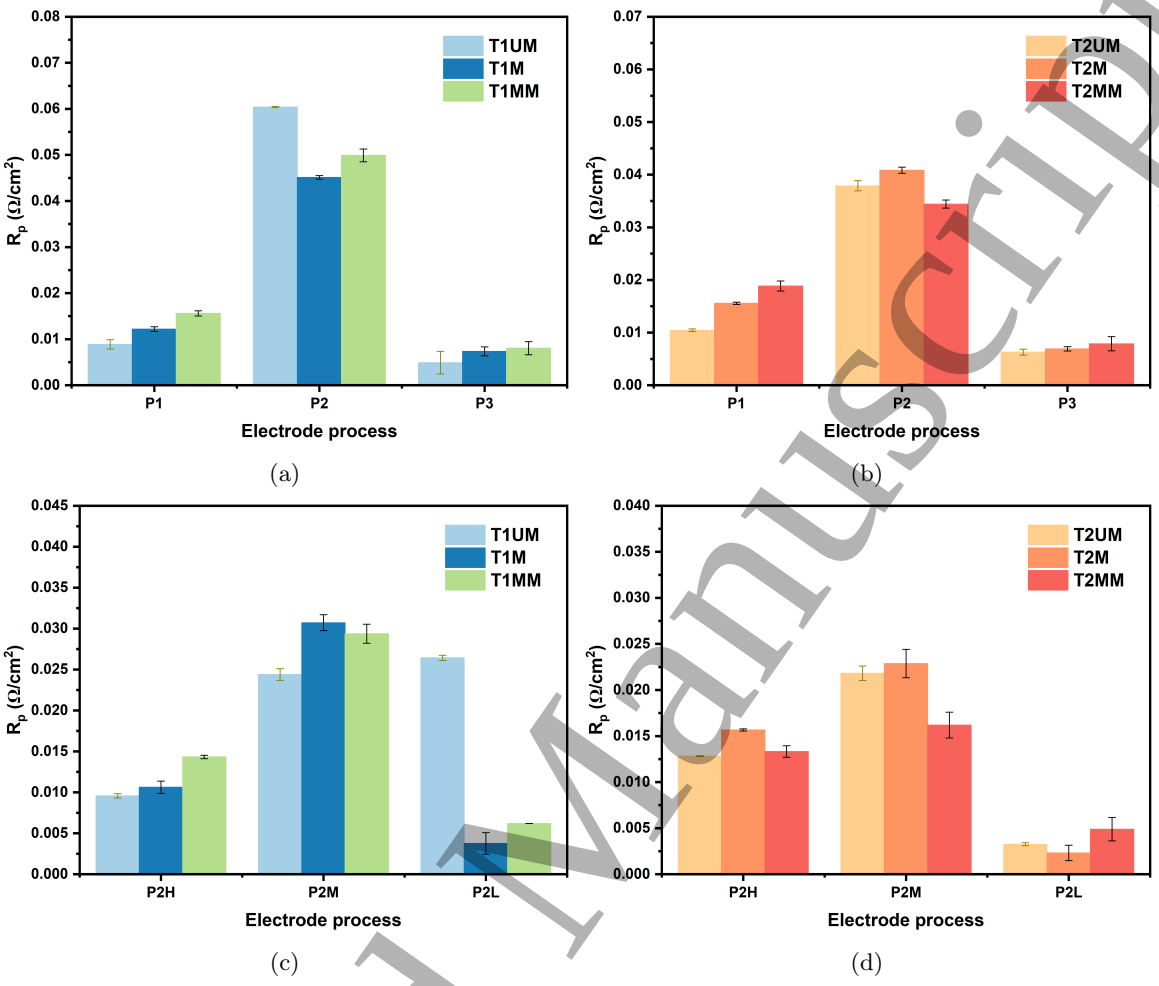

Figure 7: Polarization resistance of each process, extracted from peak fitting of distribution of relaxation time, for (a) the sample T1UM, T1M and T1MM, (b) the sample T2UM, T2M and T2MM, measured at 670 $^{\circ}C$ under pO_2 of around 0.21 atm. The sub-processes of P2 of corresponding samples, P2H, P2M and P2L, were given in (c) and (d), respectively.

Similar to the effect of electrode thickness, the smaller particle size would lead to greater resistance in processes P1 and P2H, which were related to oxygen species diffusion within the electrode. This can be explained by the tortuosity change of each phase. Considering the effective conductivity σ_{eff} of each phase, which was given by [59]:

$$\sigma_{eff} = \sigma_b(\varepsilon/\tau) \tag{4}$$

where ε and τ are the volume fraction and the tortuosity of the corresponding phase, respectively. σ_b is the bulk conductivity.

Smaller PNO particles resulted in greater tortuosity of PNO and CGPO, as shown in table. 2. Hence, the effective conductivity of each phase was reduced and led to higher diffusion resistance. According to Eq. 4, the conductivity of each conducting phase is inversely proportional to its tortuosity at a given volume fraction. Hence, the resistance of diffusion within each phase is proportional to its tortuosity considering Ohm's law:

$$R = l/\sigma_{eff} \tag{5}$$

where l is the diffusion length of conducting species. It was interesting to find that the ratio of the resistance of process P1 between sample T1UM and T1M (0.73), T2UM and T2M(0.64), were

close to the ratio of tortuosity between the unmilled CGPO phase and the milled CGPO (0.69). The slight deviation was due to the difference in l in Ohm's law. This consistency supported the assignment that process P1 was associated with oxygen ion diffusion within the CGPO phase.

It can be found that both electrode thickness and PNO particle size affected the total ASR of cells. Increasing thickness and decreasing PNO particle size caused a monotonic resistance increase in P1 and P2H. Appropriate increase of thickness and particle size reduction enhanced ORR by facilitating oxygen dissociation and reduced the total ASR although a slight resistance increase in process P1 and process P2H was present. However, both microstructural modifications simultaneously led to high resistance of process P1 and process P2H, compensating the resistance reduction in ORR. Hence, a compromise has to be made during microstructural optimization to obtain lower ASR. Over-optimized microstructures, i.e. over-increased electrode thickness and over-reduced PNO size, led to significantly high resistances of processes P1 and P2H.

4.5.3 Decoupling TPB and DPB contributions

In the following, we attempt to decouple the contribution of TPB and DPB to the ORR. From the Nyquist plot for each sample as shown in figure. 2, it was impossible to tell if TPB or DPB contributed more to ORR, or were equally important. However, the variation of ASR as a function of electrode thickness provided some information. The entire electrode of thickness 16 um was active for ORR because the resistance of process P2 reduced when the thickness increased to 36 um, for both electrodes composed of unmilled and milled PNO. It is still uncertain if the active area of electrodes was greater or smaller than 36 um. The active area for electrodes of a single mixed ionic electronic conducting (MIEC) phase in which DPB dominates is usually a few microns according to the Adler-Lane-Steel (ALS) model[20, 21]. This supported the suggestion that the TPB played a dominant role over DPB for ORR in the present case. In addition, the ALS model predicts a Gerischer behaviour for single phase MIEC electrodes. However, such a Gerischer behaviour was not observed, as shown in figure. 2.

The active area for composite electrodes is much greater than that for electrodes composed of a single MIEC phase since the addition of an ionic phase extends TPB from the electrode/electrolyte interface into the electrode as long as the conduction paths of oxide ion and electron are guaranteed. Haanappel et.al. systematically investigated the effect of cathode thickness on electrochemical performance of anode-supported single cells with $La_{0.2}Sr_{0.3}O_3$(LSM)/LSM-Y_2O_3-stablised ZrO_2 as composite cathode and found the highest current density was obtained with cathode thickness of 30 um [12]. Similar works were also carried out by Barbucci et.al. and an optimum thickness of YSZ/LSM composite electrode was found to be about 40 um[52]. Some graded composite electrodes have even higher thickness[11, 60].

To be more rigorous, the ALS model was considered here with the obtained microstructure data from FIB - SEM to evaluate if it was adaptable to the present case which involved a MIEC and an additional ionic phase, and hence, the contribution from DPB. Given the electronic conductivity and oxygen ionic conductivity of $235S\ cm^{-1}$ and $1.49\times10^{-3}S\ cm^{-1}$ for PNO under $700°C$ and pO_2 of 0.21 bar [27], respectively, PNO was considered as a good mixed electronic ionic conducting phase. CGPO was mainly acting as a good ionic conducting phase given the electronic conductivity and oxygen ionic conductivity of 0.004 $S\ cm^{-1}$ and 0.055 $S\ cm^{-1}$ under the same condition[27], respectively. The expression for the ALS model is given by:

$$R_{chem} = (\frac{RT}{2F^2})(\frac{\tau f}{(1-\varepsilon)aD^* kc_{mc}^2})^{0.5} \tag{6}$$

where R_{chem} is ASR, R is the gas constant, T is the temperature, F is the Faraday constant, τ is the tortuosity of MIEC phase, i.e., PNO, f is the Bardeen-Herring correlation factor, ε is porosity, a is the surface area, which is DPB between PNO and pore, D^* is the oxygen tracer diffusion coefficient and k is the oxygen tracer surface exchange coefficient, and c_{mc} is the concentration of oxygen sites in PNO.

The ASR calculated according to Eq. 6 was 0.40 $\Omega\ cm^2$ and 0.47 $\Omega\ cm^2$ by assuming f was unity for electrodes composed of unmilled PNO and milled PNO, respectively. (1-ε), the fraction of MIEC phase in the ALS model, was replaced by 0.3 in both cases since two solid phases which had almost the same volume fraction presented considering 40 % porosity. This prediction for the electrode composed of unmilled PNO was lower than the result obtained from Tsai who investigated unmilled PNO as a single phase electrode with a total ASR of 4.36 $\Omega\ cm^2$ under virtually the same condition [27]. This discrepancy possibly came from other processes included in the total ASR such as oxide ion transfer between the electrode and the electrolyte while the ALS model only considered surface

exchange of oxygen and solid-state diffusion in the MIEC phase (PNO in this case). The ASR was lowered to 0.25 $\Omega\ cm^2$ when 50 $wt.$ % CGPO was added into the electrode as a composite electrode [27]. The significantly lower ASR originated from the addition of the CGPO phase and confirmed that TPB was dominant in terms of the ORR. The total ASR was further reduced to 0.055 $\Omega\ cm^2$ in this study, possibly because of better microstructures including smaller PNO particles and the addition of an interlayer which is a common method for improving electrode performance [11, 14].

Considering the ALS model underestimated the performance of the composite electrodes and the assignment of each electrochemical process occurring in the electrodes, the ORR should occur at TPB with slight contribution from DPB. The enhancement in electrochemical performance due to microstructural optimization, thickness and particle size adjustments, was attributed to more TPB in electrodes.

4.6 Fuel cell performance evaluation

Electrochemical performance of the optimised composite cathode (T2UM) in an anode supported fuel cell is shown in figure 8a. It was found that the open circuit potential value was 1.026 V at an operating temperature of 800 $^{\circ}C$ which is similar to its theoretical value (1.13V) operating with 97 % H_2, 3 % H_2O as the anode gas composition and flowing air as the cathode composition. The peak power density values for this configuration were summarized in table. 4. The peak power density of 1.01 $W\ cm^{-2}$ at 800 $^{\circ}C$ is promising performance for a new cathode material tested in a thick electrolyte button cell configuration. Regarding the EIS data as shown in figure. 8b, the values of polarization resistance and the values of ohmic resistance are summarized in table. 4. Compared to the values of the polarisation resistance obtained in the symmetric cell tests it is clear that the ASR of the full-cell test was greater, which led to a lower fuel cell performance than was expected, although a total ASR of 0.28 $\Omega\ cm^2$ is a competitive value. Further optimisation of the electrolyte, anode and gas compositions would be expected to lead to further performance improvements.

Temperature ($^{\circ}C$)	650	700	750	800
Ohmic resistance ($\Omega\ cm^2$)	0.341	0.228	0.166	0.131
Polarization resistance ($\Omega\ cm^2$)	1.003	0.534	0.374	0.280
Power density ($W\ cm^{-2}$)	0.34	0.53	0.76	1.01

Table 4: The ohmic resistance, polarization resistance, and power density of the fuel cell at investigated temperatures.

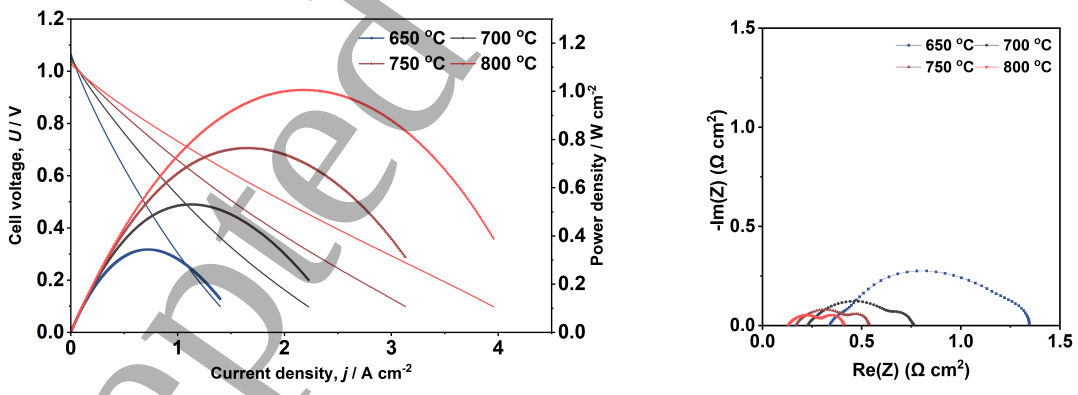

(a) (b)

Figure 8: (a) Cell voltage-current density curves and power densities-current density curves of the single cell made of unmilled PNO as the cathode and Ni - YSZ as the anode and YSZ - GDC as the electrolyte, and (b) the corresponding EIS results, at investigated temperatures.

5 Conclusion

This article reports a systematic investigation in the effects of thickness and particle size on electrochemical processes occurring in PNO - CGPO composite electrodes for IT - SOFCs. Initially, the performance was mainly restricted by oxygen dissociation which was one step of the ORR. Microstructural optimization via increasing electrode thickness and reducing electrode particle size improved electrode performance by enhancing the ORR because of the introduction of more TPB into electrodes. In the meanwhile, the resistance of diffusion of oxygen species within the electrode increased slightly. However, over-optimization led to a significant resistance increase in the diffusion of oxygen species while the ORR was not reduced further. Therefore, over-optimization has to be avoided and a trade-off between ORR and diffusion of oxygen species has to be made to achieve the best performance for this composite electrode. The lowest ASR obtained at 670 $^{\circ}C$ under pO_2 of 0.21 atm in this investigation was 0.055 $\Omega\ cm^2$ for sample T2UM. Further lower ASR is expected with the help of milled PNO if the effect in the diffusion of oxygen species was eliminated by optimizing the electrode microstructures.

The peak power density at 800 $^{\circ}C$ was 1 $W\ cm^{-2}$, which demonstrates the PNO - CGPO composite is a promising SOFC cathode material.

6 Acknowledgement

The authors gratefully acknowledge the support from Miss Baghdadi Yasmine and Dr.Jingyi Chen and Dr.Chen - Yu Tsai. The authors also gratefully acknowledge the Avizo license from Prof.Nigel Brandon.

7 ORCID iDs

Zheng Xie https://orcid.org/0009-0001-6622-538X
Inyoung Jang https://orcid.org/0000-0002-7478-8940
Mengzheng Ouyang https://orcid.org/0000-0003-4896-416X
Anna Hankin https://orcid.org/0000-0001-8358-2349
Stephen J Skinner https://orcid.org/0000-0001-5446-2647

References

[1] P.M. Falcone, M. Hiete, and A. Sapio. Hydrogen economy and sustainable development goals: Review and policy insights. *Current Opinion in Green and Sustainable Chemistry*, 31:100506, 2021.

[2] S.S. Penner. Steps toward the hydrogen economy. *Energy*, 31(1):33–43, 2006.

[3] S.C Singhal. Advances in solid oxide fuel cell technology. *Solid State Ionics*, 135(1):305–313, 2000.

[4] N. Jaiswal, K. Tanwar, R. Suman, D. Kumar, S. Upadhyay, and O. Parkash. A brief review on ceria based solid electrolytes for solid oxide fuel cells. *Journal of Alloys and Compounds*, 781:984–1005, 2019.

[5] E. Ivers-Tiffée, A. Weber, and D. Herbstritt. Materials and technologies for SOFC-components. *Journal of the European Ceramic Society*, 21(10):1805–1811, 2001.

[6] J. Kilner, S. Skinner, S. Irvine, and P. Edwards. *Functional Materials for Sustainable Energy Applications*, volume 35. Elsevier Science Technology, 2012.

[7] I. Jang and G.H. Kelsall. Fabrication of 3D NiO-YSZ structures for enhanced performance of solid oxide fuel cells and electrolysers. *Electrochemistry Communications*, 137:107260, 2022.

[8] N.H Menzler, F. Tietz, S. Uhlenbruck, H.P. Buchkremer, and D. Stöver. Materials and manufacturing technologies for solid oxide fuel cells. *Journal of Materials Science*, 45:3109–3135, 2010.

[9] T. Kenjo and M. Nishiya. $LaMnO_3$ air cathodes containing ZrO_2 electrolyte for high temperature solid oxide fuel cells. *Solid State Ionics*, 57(3):295–302, 1992.

[10] T. Kenjo, S. Osawa, and K. Fujikawa. High temperature air cathodes containing ion conductive oxides. *Journal of The Electrochemical Society*, 138(2):349–355, 1991.

[11] R. Woolley and S. Skinner. Functionally graded composite $La_2NiO_{4+\delta}$ and $La_4Ni_3O_{10-\delta}$ solid oxide fuel cell cathodes. *Solid State Ionics*, 255:1–5, 2014.

[12] V.A.C. Haanappel, J. Mertens, D. Rutenbeck, C. Tropartz, W. Herzhof, D. Sebold, and F. Tietz. Optimisation of processing and microstructural parameters of lsm cathodes to improve the electrochemical performance of anode-supported SOFCs. *Journal of Power Sources*, 141(2):216–226, 2005.

[13] R. K. Sharma, M. Burriel, and E. Djurado. $La_4Ni_3O_{10-\delta}$ as an efficient solid oxide fuel cell cathode: electrochemical properties versus microstructure. *J. Mater. Chem. A*, 3:23833–23843, 2015.

[14] N. Hildenbrand, P. Nammensma, D.H.A. Blank, H.J.M. Bouwmeester, and B.A. Boukamp. Influence of configuration and microstructure on performance of $La_2NiO_{4+\delta}$ intermediate-temperature solid oxide fuel cells cathodes. *Journal of Power Sources*, 238:442–453, 2013.

[15] R. Hui, Z. Wang, O. Kesler, L. Rose, J. Jankovic, S. Yick, R. Maric, and D. Ghosh. Thermal plasma spraying for SOFCs: Applications, potential advantages, and challenges. *Journal of Power Sources*, 170(2):308–323, 2007.

[16] S. Uhlenbruck, N. Jordan, D. Sebold, H.P. Buchkremer, V.A.C. Haanappel, and D. Stöver. Thin film coating technologies of $(Ce,Gd)O_{2-\delta}$ interlayers for application in ceramic high-temperature fuel cells. *Thin Solid Films*, 515(7):4053–4060, 2007.

[17] A. Flura, C. Nicollet, V. Vibhu, A. Rougier, J. Bassat, and J. Grenier. Ceria doped with praseodymium instead of gadolinium as efficient interlayer for lanthanum nickelate SOFC oxygen electrode. *Electrochimica Acta*, 231:103–114, 2017.

[18] C. Rossignol, J.M. Ralph, J.-M. Bae, and J.T. Vaughey. $Ln_{1-x}Sr_xCoO_3$ (Ln=Gd, Pr) as a cathode for intermediate-temperature solid oxide fuel cells. *Solid State Ionics*, 175(1):59–61, 2004.

[19] A. Orera and P. R. Slater. New chemical systems for solid oxide fuel cells. *Chemistry of Materials*, 22(3):675–690, 2010.

[20] S. B. Adler, J. A. Lane, and B. C. H. Steele. Electrode kinetics of porous mixed-conducting oxygen electrodes. *Journal of The Electrochemical Society*, 143(11):3554–3564, 1996.

[21] S. B. Adler. Factors governing oxygen reduction in solid oxide fuel cell cathodes. *Chemical Reviews*, 104(10):4791–4844, 2004.

[22] P. Laffez, Q. Simon, Y. Kikuchi, R. Retoux, F. Giovannelli, and A. Yamamoto. Growth of polycrystalline $Pr_4Ni_3O_{10}$ thin films for intermediate temperature solid oxide fuel cell cathode by radio frequency magnetron co-sputtering. *Thin Solid Films*, 693:137705, 2020.

[23] J.M. Bassat, C. Allançon, P. Odier, J.P. Loup, M. Deus Carvalho, and A. Wattiaux. Electronic properties of $Pr_4Ni_3O_{10\pm\delta}$. *European Journal of Solid State and Inorganic Chemistry*, 35(2):173–188, 1998.

[24] C.Y. Tsai, A. Aguadero, and S. Skinner. High electrical conductivity and crystal structure of the solid oxide cell electrode $Pr_4Ni_3O_{10-\delta}$. *Journal of Solid State Chemistry*, 289:121533, 2020.

[25] V. Vibhu, A. Rougier, C. Nicollet, A. Flura, S. Fourcade, N. Penin, J. Grenier, and J. Bassat. $Pr_4Ni_3O_{10+\delta}$: A new promising oxygen electrode material for solid oxide fuel cells. *Journal of Power Sources*, 317:184–193, 2016.

[26] S. Cheng, C. Chatzichristodoulou, M. Søgaard, A. Kaiser, and P.V. Hendriksen. Ionic/Electronic Conductivity, Thermal/Chemical Expansion and Oxygen Permeation in Pr and Gd Co-Doped Ceria $Pr_xGd_{0.1}Ce_{0.9-x}O_{1.95-\delta}$. *Journal of The Electrochemical Society*, 164(13):F1354–F1367, 2017.

[27] C.Y. Tsai. *Phase evolution and reactivity of $Pr_2NiO_{4+\delta}$ and $Ce_{0.9}Gd_{0.1}O_{2-\delta}$ solid oxide cell electrodes*. PhD thesis, Imperial College London, 2020.

[28] S.J. Cooper, A. Bertei, P.R. Shearing, J.A. Kilner, and N.P. Brandon. Taufactor: An open-source application for calculating tortuosity factors from tomographic data. *SoftwareX*, 5:203–210, 2016.

[29] I. Jang, C. Kim, S. Kim, and H. Yoon. Fabrication of thin films on an anode support with surface modification for high-efficiency intermediate-temperature solid oxide fuel cells via a dip-coating method. *Electrochimica Acta*, 217:150–155, 2016.

[30] B. Timurkutluk, Y. Ciflik, T. Altan, and O. Genc. Synthetical designing of solid oxide fuel cell electrodes: Effect of particle size and volume fraction. *International Journal of Hydrogen Energy*, 47(73):31446–31458, 2022.

[31] B. Kenney, M. Valdmanis, C. Baker, J.G. Pharoah, and K. Karan. Computation of TPB length, surface area and pore size from numerical reconstruction of composite solid oxide fuel cell electrodes. *Journal of Power Sources*, 189(2):1051–1059, 2009.

[32] A.Z. Lichtner, D. Jauffrès, D. Roussel, F. Charlot, C.L. Martin, and R.K. Bordia. Dispersion, connectivity and tortuosity of hierarchical porosity composite SOFC cathodes prepared by freeze-casting. *Journal of the European Ceramic Society*, 35(2):585–595, 2015.

[33] B. Völker and R.M. McMeeking. Impact of particle size ratio and volume fraction on effective material parameters and performance in solid oxide fuel cell electrodes. *Journal of Power Sources*, 215:199–215, 2012.

[34] A. Esquirol, N. P. Brandon, J. A. Kilner, and M. Mogensen. Electrochemical characterization of $La_{0.6}Sr_{0.4}Co_{0.2}Fe_{0.8}O_3$ cathodes for intermediate-temperature SOFCs. *Journal of The Electrochemical Society*, 151(11):A1847, 2004.

[35] Y. Takeda, R. Kanno, M. Noda, Y. Tomida, and O. Yamammto. Cathodic polarization phenomena of perovskite oxide electrodes with stabilized zirconia. *Journal of the Electrochemical Society*, 134(11):2656–2661, 1987.

[36] S.B. Adler, X.Y. Chen, and J.R. Wilson. Mechanisms and rate laws for oxygen exchange on mixed-conducting oxide surfaces. *Journal of Catalysis*, 245(1):91–109, 2007.

[37] M. Schönleber, D. Klotz, and E. Ivers-Tiffée. A method for improving the robustness of linear kramers-kronig validity tests. *Electrochimica Acta*, 131:20–27, 2014.

[38] B.A. Boukamp. A linear kronig-kramers transform test for immittance data validation. *Journal of The Electrochemical Society*, 142(6):1885, 1995.

[39] S. Dierickx, A. Weber, and E. Ivers-Tiffée. How the distribution of relaxation times enhances complex equivalent circuit models for fuel cells. *Electrochimica Acta*, 355:136764, 2020.

[40] M.J. Escudero, A. Aguadero, J.A. Alonso, and L. Daza. A kinetic study of oxygen reduction reaction on La_2NiO_4 cathodes by means of impedance spectroscopy. *Journal of Electroanalytical Chemistry*, 611(1):107–116, 2007.

[41] J. Yan, Z. Zhao, L. Shang, D. Ou, and M. Cheng. Co-synthesized Y-stabilized Bi_2O_3 and sr-substituted $LaMnO_3$ composite anode for high performance solid oxide electrolysis cell. *Journal of Power Sources*, 319:124–130, 2016.

[42] F. Mauvy, C. Lalanne, J. Bassat, J. Grenier, H. Zhao, L. Huo, and P. Stevens. Electrode properties of $Ln_2NiO_{4+\delta}$ (Ln=La, Nd, Pr): Ac impedance and dc polarization studies. *Journal of The Electrochemical Society*, 153(8):A1547, 2006.

[43] A. Jais, S.A.M Ali, M. Anwar, M.R Somalu, A. Muchtar, W.N.R.W Isahak, C.Y. Tan, R. Singh, and N.P. Brandon. Enhanced ionic conductivity of scandia-ceria-stabilized-zirconia (10Sc1CeSZ) electrolyte synthesized by the microwave-assisted glycine nitrate process. *Ceramics International*, 43(11):8119–8125, 2017.

[44] A.R. Gilev, E.A. Kiselev, M.E. Ozhiganov, and V.A. Cherepanov. Polarization resistance of the ruddlesden-popper nickelates $La_{n+1}Ni_nO_{3n+1}$ (n = 1, 2, 3): Comparative analysis using the distribution of relaxation times method. *Solid State Ionics*, 386:116032, 2022.

[45] V. Sonn, A. Leonide, and E. Ivers-Tiffée. Combined Deconvolution and CNLS Fitting Approach Applied on the Impedance Response of Technical Ni/8YSZ Cermet Electrodes. *Journal of The Electrochemical Society*, 155(7):B675, 2008.

[46] M. Riegraf, R. Costa, G. Schiller, K.A Friedrich, S. Dierickx, and A. Weber. Electrochemical Impedance Analysis of Symmetrical Ni/Gadolinium-Doped Ceria (CGO10) Electrodes in Electrolyte-Supported Solid Oxide Cells. *Journal of The Electrochemical Society*, 166(13):F865, 2019.

[47] Y.L. Huang, M. Hussain, I.A. Robinson, and E.D. Wachsman. Nanointegrated, high-performing cobalt-free bismuth-based composite cathode for low-temperature solid oxide fuel cells. *ACS Applied Materials & Interfaces*, 10(34):28635–28643, 2018.

[48] J.T. Irvine, D.C. Sinclair, and A.R. West. Electroceramics: Characterization by impedance spectroscopy. *Advanced Materials*, 2(3):132–138, 1990.

[49] B.C.H. Steele. Appraisal of $Ce_{1-y}Gd_yO_{2-y/2}$ electrolytes for IT-SOFC operation at 500 °C. *Solid State Ionics*, 129(1):95–110, 2000.

[50] C.W. Tanner, K. Fung, and A.V. Virkar. The effect of porous composite electrode structure on solid oxide fuel cell performance: I. theoretical analysis. *Journal of The Electrochemical Society*, 144(1):21–30, 1997.

[51] V. Dusastre and J.A. Kilner. Optimisation of composite cathodes for intermediate temperature SOFC applications. *Solid State Ionics*, 126(1):163–174, 1999.

[52] A. Barbucci, M. Carpanese, A.P. Reverberi, G. Cerisola, M. Blanes, P.L. Cabot, M. Viviani, A. Bertei, and C. Nicolella. Influence of electrode thickness on the performance of composite electrodes for SOFC. *Journal of Applied Electrochemistry*, 38(2):939–945, 2008.

[53] M. Koyama, C.J. Wen, T. Masuyama, J. Otomo, H. Fukunaga, K. Yamada, K. Eguchi, and H. Takahashi. The mechanism of porous $Sm_{0.5}Sr_{0.5}CoO_3$ cathodes used in solid oxide fuel cells. *Journal of The Electrochemical Society*, 148(7):A795, 2001.

[54] K. Sasaki, J.-P. Wurth, R. Gschwend, M. Gödickemeier, and L. J. Gauckler. Microstructure-property relations of solid oxide fuel cell cathodes and current collectors: Cathodic polarization and ohmic resistance. *Journal of The Electrochemical Society*, 143(2):530–543, 1996.

[55] T. Tsai and S.A. Barnett. Effect of LSM-YSZ cathode on thin-electrolyte solid oxide fuel cell performance. *Solid State Ionics*, 93(3):207–217, 1997.

[56] M.J.L. Østergård, C. Clausen, C. Bagger, and M. Mogensen. Manganite-zirconia composite cathodes for SOFC: Influence of structure and composition. *Electrochimica Acta*, 40(12):1971–1981, 1995.

[57] S. H. Chan and Z. T. Xia. Anode micro model of solid oxide fuel cell. *Journal of The Electrochemical Society*, 148(4):A388, 2001.

[58] D. Chen, W. Bi, W., and Z. Lin. Combined micro-scale and macro-scale modeling of the composite electrode of a solid oxide fuel cell. *Journal of Power Sources*, 195(19):6598–6610, 2010.

[59] A. Atkinson, S.A. Baron, and N.P. Brandon. Ac impedance spectra arising from mixed ionic electronic solid electrolytes. *Journal of The Electrochemical Society*, 151(5):E186, 2004.

[60] P. Holtappels and C. Bagger. Fabrication and performance of advanced multi-layer SOFC cathodes. *Journal of the European Ceramic Society*, 22(1):41–48, 2002.